



## **Final Draft of the original manuscript**

Lazurenko, D.; Laptev, I.; Golkovsky, M.; Stark, A.; Paul, J.; Bataev, I.; Ruktuev, A.; Song, L.; Gollwitzer, C.; Pyczak, F.:

**Influence of the Ti/Al/Nb ratio on the structure and properties on intermetallic layers obtained on titanium by non-vacuum electron beam cladding.**

In: Materials Characterization. Vol. 163 (2020) 110264.

First published online by Elsevier: 03.03.2020

<https://dx.doi.org/10.1016/j.matchar.2020.110246>

# Influence of the Ti/Al/Nb ratio on the structure and properties on intermetallic layers obtained on titanium by non-vacuum electron beam cladding

Daria V. Lazurenko<sup>1\*</sup>, Ilia S. Laptev<sup>1</sup>, Mikhail G. Golkovsky<sup>2</sup>, Andreas Stark<sup>3</sup>, Jonathan Paul<sup>3</sup>, Ivan Bataev<sup>1</sup>, Alexey A. Ruktuev<sup>1</sup>, Lin Song<sup>4</sup>, Christian Gollwitzer<sup>5</sup>, Florian Pyczak<sup>3</sup>

<sup>1</sup> Novosibirsk State Technical University, Karl Marks av. 20, 630073, Novosibirsk, Russia

<sup>2</sup> Budker Institute of Nuclear Physics of Siberian Branch Russian Academy of Sciences 630090 Russia Novosibirsk Lavrentiev av. 11

<sup>3</sup> Helmholtz Zentrum Geesthacht, Max-Planck-Straße 1, 21502 Geesthacht, Germany

<sup>4</sup> Northwestern Polytechnical University, 127#Youyi western Road Xi'an. 710072.P.R. China

<sup>5</sup> Physikalisch-Technische Bundesanstalt (PTB), Abbestr. 2-12, 10587 Berlin, Germany

\*corresponding author: [pavlyukova\\_87@mail.ru](mailto:pavlyukova_87@mail.ru)

## Abstract

Ti-Al-Nb based intermetallic layers of sufficient quality and thickness were obtained by non-vacuum electron beam cladding on the surfaces of Ti workpieces. Optical microscopy and X-ray tomography did not reveal any dramatical defects in the structure of cladded layers. X-ray diffraction as well as scanning and transmission electron microscopy were applied to thoroughly investigate the structure and phase composition of coatings. It was found that non-equilibrium cooling conditions of coatings provided by fast removal of heat to untreated Ti substrate after the electron beam cladding was terminated induced the proceeding of metastable phase transformations. For example,  $\gamma$ -phase formation was suppressed in these coatings. In coatings with 8 and 20 at. % Nb (46 and 43 % Al respectively) along with ordered with  $\alpha_2$ , formation of disordered solution of the alloying elements in  $\alpha$ -Ti took place. In high-Nb alloys  $\beta$ (B2) phase has undergone the diffusionless transformation to  $\omega'$ , which is the intermediate phase in  $\beta \rightarrow \omega$  and the coating with the maximum Nb content characterized by appearance of  $\gamma_1$  as a main phase.  $\omega$ -phase had negative influence to hardness and wear resistance of coatings, however, generally this parameter increased in 1.3-1.75 times compared to cp-Ti. The high temperature creep and oxidation properties decreased proportionally with increasing Nb and decreasing Al content in the cladded layers.

**Keywords:** electron beam cladding; titanium aluminides; metastable phases; diffraction analysis; wear; high-temperature properties

## 1. Introduction

Titanium and its alloys are important structural materials that are widely used in aircraft manufacture, rocketry, chemical engineering and other important areas of industry which require components with high specific strength and corrosion resistance. However, at elevated temperatures, a number of difficulties concerning the exploitation of titanium parts arise. For example, titanium possesses low creep and also low oxidation resistance due to its reactivity with atmospheric gases and can thus only be used at temperatures below 350 °C [1]. This problem can be solved by the introduction of intermetallic phases into the structure of titanium. Nowadays a number of heat and creep resistant titanium alloys, which are able to withstand high-temperature loading, have been developed [1]. Nevertheless, the most efficient way to retain the high-temperature loss of properties due to reactions with the surrounding atmosphere is via protective coatings. Such coatings may protect the base material from degradation due to oxidation and also

improve the tribological properties of titanium alloys, which typically possess a low resistance to any type of wear. Thus, the formation of intermetallics on the surface of titanium parts could increase their performance and extend the area of application opportunities.

Coating titanium with titanium aluminides is rather simple due to the fact that aluminum and titanium readily react with each other producing intermetallic structures [2]. The cladding of titanium workpieces with titanium aluminides is widely discussed in the literature. Two widespread technologies used are (i) aluminizing [3-10] and (ii) the application of aluminum or a mixture of titanium and aluminum [11-15] powders to the surfaces of titanium parts. Both methods require subsequent heat treatment to produce a solid intermetallic layer on the workpiece ( excepting application of a pre-alloyed intermetallic powder [16]). The most efficient coating technologies are high energy methods, such as laser cladding [11, 12, 16-18] or electron beam cladding [19, 20]. These methods allow the fast production of cladded layers with a thickness of up to 2 mm. Electron beam cladding is preferred to laser cladding with respect to process efficiency. Electron beam is characterized by a higher penetration depth and provides more homogeneous heating of surface layers of the material [21]. Moreover, in the case of electron beam cladding there is no problem of beam reflection from the surface of the metal workpiece. Thus, one could expect that the application of electron beam cladding may be an efficient way to produce thick intermetallic coatings on a titanium surface by melting a powder mixture that is distributed on the surface of the workpiece.

In previous studies [19, 20] we found that non-vacuum electron beam cladding of titanium and aluminum powders to a titanium substrate led to coatings containing the  $\gamma$ -TiAl and  $\alpha_2$ -Ti<sub>3</sub>Al phases. Compared to commercially pure (cp) titanium, these coatings possessed higher hardness and oxidation resistance. However, the high brittleness of intermetallic compounds led to the formation of cracks during the early stages of fabrication [20]. Decreasing the aluminum fraction in the initial powder mixture prevented active cracking, but also reduced the oxidation resistance.

Alloying is an efficient approach to increase the crack growth resistance and the oxidation and creep resistance of Ti-Al intermetallic alloys [22]. For example, the addition of only 2 at. % of the alloying element (Nb, Cr, Mn, etc.) to the Ti-48Al binary composition improves high-temperature behavior and provides reasonable room-temperature ductility. Highly alloyed Ti-Al-based intermetallics are also widely discussed in the literature. Alloys with a high level of Nb has a special significance. Such alloys demonstrate high strength combined with good creep and oxidation resistance. Consequently, coating with titanium aluminide alloyed with Nb seems a reasonable way to improve the physical, chemical and mechanical properties of the coating.

The aim of this study was the fabrication of Nb-alloyed Ti-Al-based coatings on cp-Ti workpieces, and the investigation of their structure and service characteristics in relation to the Nb, Al and Ti content.

## 2. Materials and methods

Cp-Ti (0.086 wt. % Fe, 0.017 wt. % Cr, 0.016 wt. % Ni, 0.012 wt. % V, 0.011 wt. % C) workpieces with dimensions of 100×50×12 mm<sup>3</sup> that had been cut from plate by waterjet cutting were used as substrates. The top surface of the workpieces was preliminary milled to remove surface oxides. Several different powder mixtures consisting of Al, Ti, Nb and flux (LiF) powders were homogeneously distributed on the top surfaces of the workpieces (Table 1). Due to the dilution of alloying elements by the base material which results from the melt of titanium surface layers occurring along with melting the powders applied to the surface during electron beam exposure, the mass fractions of alloying components (Al and Nb) in powder mixtures were

1.5-fold higher than that in the alloy designation. The mass of powder per area used was 0.45 g/cm<sup>2</sup>.

Table 1. Samples notation and corresponding the starting powder mixtures used for the electron beam cladding.

Sample designation (a fraction of alloying elements calculated to at. %)	Mass of the elements in a starting powder mixture (wt. %)			
	Ti	Al	Nb	LiF (flux)
Ti-48Al-2Nb	12	33	5	50
Ti-46Al-8Nb	5	28	17	50
Ti-43Al-14Nb	-	24	27	49
Ti-40Al-20Nb	-	20	34	46

The cladding was carried out at the Budker Institute of Nuclear Physics (SB RAS, Novosibirsk, Russia) using an ELV-6 industrial electron accelerator to provide the electron beam. The main advantage of the ELV-6 equipment is the possibility to inject a concentrated beam of electrons with an energy of 1.4 MeV and a power up to 100 kW in an air atmosphere. Normal accelerators with an electron energy of 20-200 keV can only be operated in vacuum due to the short electron track length in air (up to 25 cm). Increasing the electron energy to above 1 MeV and the incorporation of an extraction device that separates the vacuum chamber of the electron beam acceleration system from the atmosphere allowed the electron beam to be injected into air. An electron energy of 1.4 MeV results in a 6 m pass length, this distance represents the distance where the electrons are completely absorbed/scattering by the air nuclei. This equipment allowed the experiments to be carried out under normal atmospheric pressure and has advantages such as reducing the complicity and duration of the cladding procedure and not restricting the dimensions of the treated workpiece (due to absence of a vacuum chamber). To protect the powders from oxidation, flux (LiF) was used. LiF melts at low temperatures, and weighing less than powder mixtures, it comes up to the surface and form the protective melted layer which prevents metallic powders from interaction with oxygen. A more detailed description of the accelerator and the principles of its operation is provided elsewhere [20, 21].

The electron beam current was the same for all experiments and was equal to 20 mA. The samples were moved under the electron beam at a rate of 10 mm/s. The beam was scanned perpendicular to the direction of sample motion with a frequency of 50 Hz and amplitude of  $\pm 25$  mm to improve the homogeneity of the heat input and increase the process efficiency. The distance from the beam outlet to the sample was 90 mm. A diameter of an electron beam at this distance was approximately 10 mm. The power of the electron beam was 28 kW, energy density for aforementioned conditions was 5.6 kJ/cm<sup>2</sup>.

The microstructure characterization samples were prepared according to a standard method. Cross sections were cut from the workpieces using a Struers Discotom-65 machine. These samples were mounted in polymer using a Buehler SimpliMet 1000 hydraulic press device.

The surface of the samples was ground using abrasive papers with a grain size ranging from 250 to 5  $\mu\text{m}$  and then using alumina with a grain size of 3  $\mu\text{m}$ . The final polishing was performed using a colloidal silica solution (0.04  $\mu\text{m}$ ) with addition of H<sub>2</sub>O<sub>2</sub> and a Kroll solution (92 % H<sub>2</sub>O, 6 % HNO<sub>3</sub>, 2 % HF).

Optical metallography was performed with a Carl Zeiss Axio Observer Z1m microscope. Images were acquired using an AxioCam MRc5 camera. Detailed microstructural analysis was carried out with a LEO Gemini 1530 scanning electron microscope (SEM) equipped with an energy dispersive X-ray (EDX) analyzer to determine the composition of local areas of material.

The fine structure within the microstructure was studied using a Philips CM200 transmission electron microscope (TEM). TEM samples were prepared by mechanical thinning 3 mm diameter specimens to a thickness of 100  $\mu\text{m}$  and subsequent twin-jet electrolytic polishing using a Fischione Model 120 device with a solution of 18 ml perchloric acid, 430 ml methanol and 250 ml 2-buthanol at a temperature of  $-39\text{ }^\circ\text{C}$  and a voltage of 30 V.

The phases within the materials were studied using synchrotron X-ray diffraction (XRD). Diffraction experiments were made at the Petra III synchrotron radiation source of the German Electron Synchrotron (Deutsches Elektronen-Synchrotron – DESY) using the High Energy Materials Science Beamline (P07) operated by Helmholtz-Zentrum Geesthacht. The radiation energy was 100 keV which corresponded to a wavelength of 0.124  $\text{\AA}$ . The spot size was  $1 \times 1$  mm. Diffraction rings were recorded in transmission using a Perkin Elmer XRD1621 2D detector with a resolution of  $2048 \times 2048$  pixels and a pixel size of  $200 \times 200\ \mu\text{m}^2$ . The sample-to-detector distance was 1927 mm. The 2D Debye-Sherrer ring patterns were azimuthally integrated providing Intensity against  $2\theta$  diffraction patterns. To analyze the phases of the oxide scales obtained after oxidation tests, an ARL X'TRA laboratory diffractometer was used.

X-ray microtomography ( $\mu\text{CT}$ ) was carried out at the Bundesanstalt für Materialforschung und -prüfung in Berlin using a self-built tomography device equipped with a 320 kV Nikon X-ray tube and Perkin-Elmer 4k PE 1611 CP3 flat panel detector with a resolution of 0.1 mm and  $4096 \times 4096$  pixels. 3000 projections were taken over an angular range of  $360^\circ$ . The 3D image reconstruction was performed using the Feldkamp algorithm [23] resulting in a 3D volume with a resolution of 5.4  $\mu\text{m}$ . This volume was then binned down to a voxel size of 21.7  $\mu\text{m}$  and imported into VGStudio MAX 3.2 for visualization and further analysis.

To determine the hardness of the samples a Wolpert Group 402 MVD microindentation tester was used. The load on the diamond indenter was 0.2 kg. Wear resistance was determined based on a friction test against fixed abrasive particles. Specimens with a diameter of 2 mm and a length of 12 mm were prepared for the test. They were cut out with the cylindrical axis perpendicular to the interface between the base material and clad layer. The clad layers were subjected to friction and measurements were carried out according to GOST 17367-71. Alundum P180 sandpaper was used as an abrasive material. The samples were placed in a holder and forced against the alundum disc with a load of 3 N. The test duration was 60 s, with the disk rotating at 60 rpm. The sample moved relatively to the disk forming Archimedes spiral trajectory. Cp-Ti was used as a reference material and its wear resistance was taken to be 1. Relative wear resistance of the cladding was calculated using the following equation:

$$\varepsilon = \frac{\Delta m_r}{\Delta m_i} \cdot \frac{\rho_i}{\rho_r}, \quad (1)$$

where  $\rho_i$  and  $\rho_r$  are densities of the investigated material and the reference material respectively;  $\Delta m_r$  and  $\Delta m_i$  are mass losses from the reference sample and the investigated sample. The density of the samples was determined by hydrostatic weighing.

Before the oxidation tests were performed, the clad layers were cut away from the substrate, thus allowing the influence of the titanium substrate on the oxidation characteristics of the coating to be excluded. The size of oxidation specimens was  $1 \times 10 \times 10\ \text{mm}^3$ . The specimens were ground using abrasive paper (P1000) and cleaned with acetone. The prepared specimens were placed into corundum crucibles and heated in a furnace up to  $900\text{ }^\circ\text{C}$  in an air atmosphere. Every 20 hours the samples were removed from the furnace, allowed to cool down and weighted using scales with a precision of  $10^{-4}$  g. Ten testing cycles were performed in this manner, leading to total oxidation time of 200 hours. Mass gain per unit area ( $\Delta m$ ) was calculated as follows:

$$\Delta m = \Delta w / s, \quad (2)$$

where  $\Delta w$  is the mass change after every cycle of testing (mg),  $s$  is the initial area of the sample ( $\text{cm}^2$ ). An oxidation test was also done using Cp-Ti which is used as a reference.

To investigate the influence of the alloying elements content on the high-temperature properties under mechanical loading, creep tests were performed using a SATEC mentor M3 testing setup. Cylindrical specimens, with a diameter of 1.5 mm and a length of 2.3 mm, were cut out from the cladded layer in the direction perpendicular to scanning, the axis of the cylinders being parallel to the surface of the specimen. A compressive load of 250 MPa was applied to the samples at 800 °C in air.

### **3. Results and discussion**

#### **3.1. Characterization of structure and phases within the materials**

##### **3.1.1. Microstructural analysis of the samples**

The quality of the cladding and underlying substrate was investigated using optical microscopy and X-ray tomography. Figure 1 shows the typical microstructure of the titanium substrate with Ti-46Al-8Nb and Ti-40Al-20Nb cladding layers. Three main zones can be distinguished in the materials: (1) the cladded layer, (2) a heat affected zone, and (3) the base material.

It seems that increasing the Nb and decreasing Al content of the coating tends to decrease the size of the heat affected zone. This phenomenon is related to the depth to which the titanium substrate is heated, which is defined by the electron beam penetration depth. A calculation of the electron energy loss intensity curves, shown in Fig. 2, was done using the method suggested by Tabata and Ito [24]. The figure shows, that the depth corresponding to the maximum of energy release gradually decreases with increasing Nb content due to the high electron density contributed by Nb atoms compared to Ti and Al in the cladded layer. At the same time, Al content (possessing lower electron density) decreases in high-niobium alloys, which also contributes in increase of the summarized electron density. Consequently, the electron beam penetration depth decreases with increase of the total electron density of a treated material, which, in turn, affects the depth to which materials is heated: the lower the electron depth penetration, the lower the heated layer thickness and the smaller the size of the heat affected zone.

It should be noted that Nb additions positively influenced the quality of the cladded layers: there were no cracks in the structure of ternary Ti-Al-Nb coatings in comparison to binary Ti-Al coatings studied previously [20].

An important issue related to cladding technologies is formation of residual stresses which appear due to the difference in temperatures and coefficients of thermal expansion between the substrate and the cladded layer. To the best of our knowledge, no experimental or computation data on residual stresses in electron beam cladded layers were reported so far. However, some simple prediction may be inferred from the data which was reported on related processes. Since the substrate during the cladding is much colder than the cladded layer its compression during the cooling stage is less and, therefore, it induces the tensile residual stresses in the cladded layer which was proven for laser cladding or weld cladding by numerical simulation or various experimental studies [25-28]. However, the exact distribution of residual stresses strongly depends on the temperature distribution during the cladding, the geometry of the cladded layer and the substrate and the properties of materials.

The electron beam melting (EBM) processes applied for layer by layer building of the structural components does not induce significant residual stresses in the samples after the treatment [29, 30]. However, the EBM process typically implies preheating of a substrate and slow cooling. Moreover, cyclical thermal exposure of an electron beam on a material, while building each new layer, contributes to cyclic formation and relaxation of residual stresses. In our case the treatment conditions were different (single pass of the electron beam and rapid

cooling of a built-up layer due to a heat conduction to the direction of a substrate) and can be rather comparable with the electron beam welding.

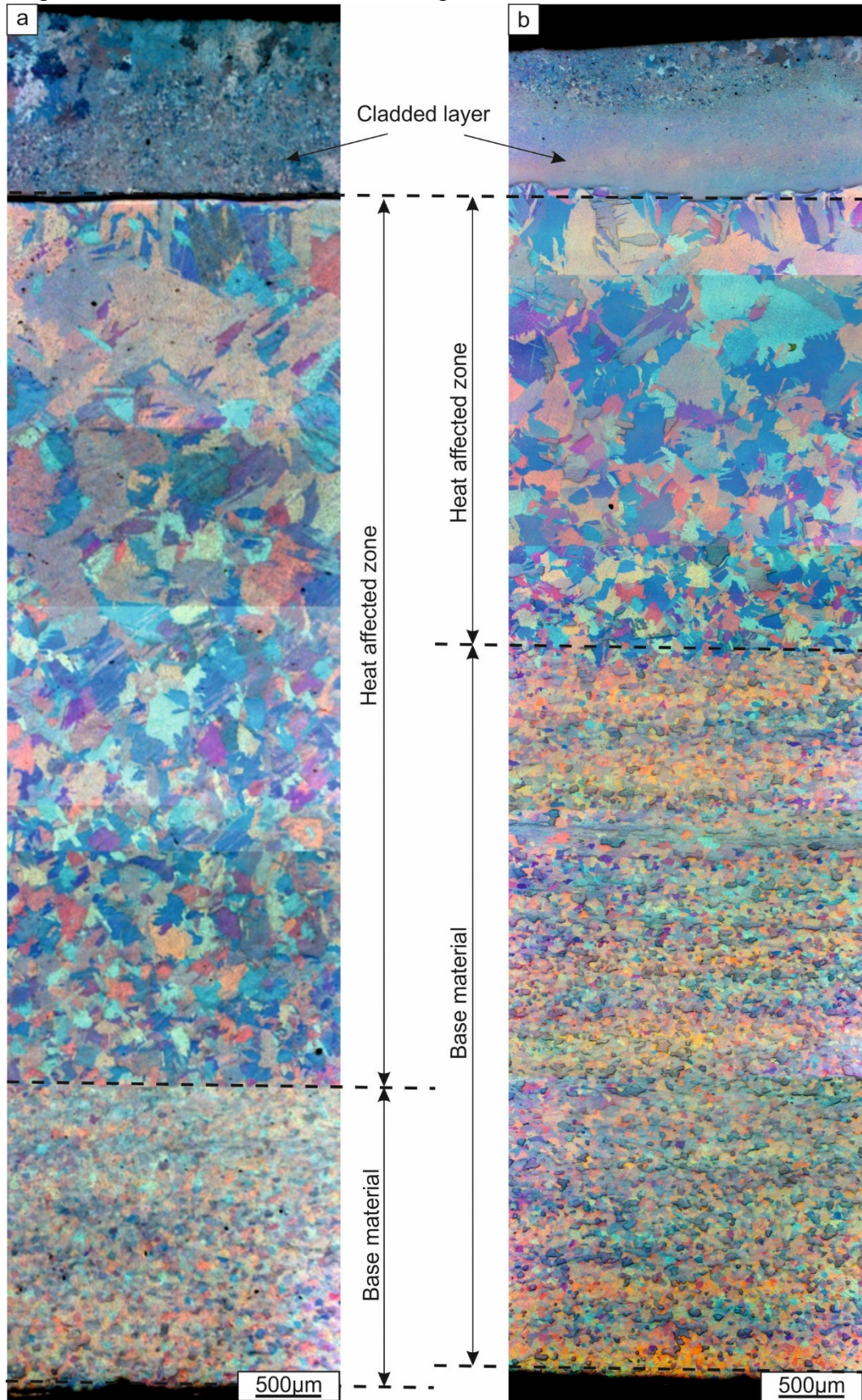


Fig. 1. The structure of surface cladded samples: a - Ti-46Al-8Nb; b - Ti-40Al-20Nb.

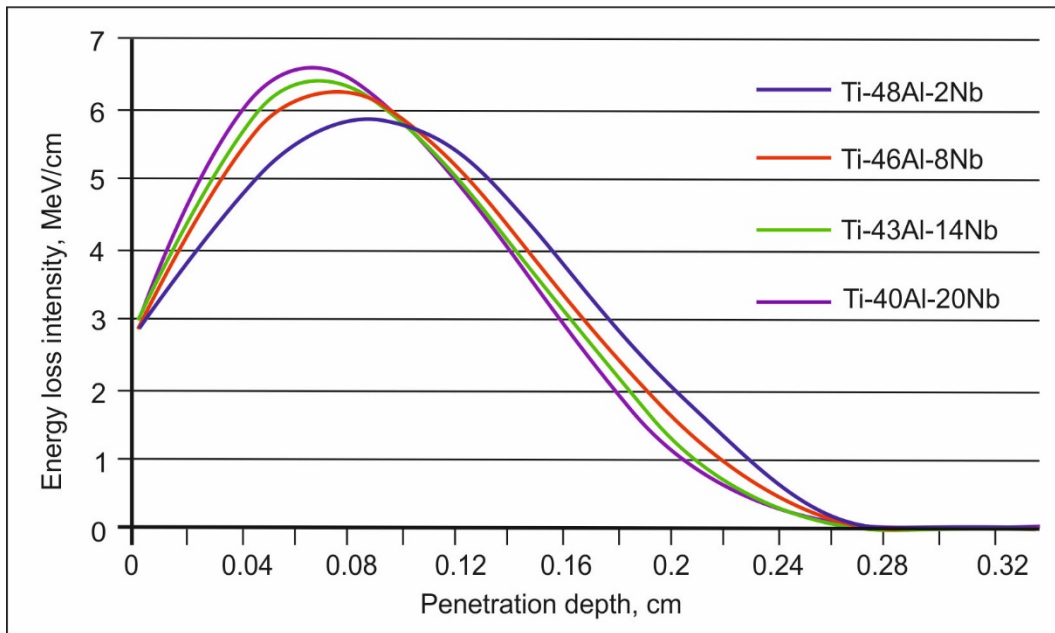


Fig. 2. Graphs illustrating the ratio between the energy release and a depth of the electron beam penetration calculated according to [24]

It is mentioned in the literature that the electron beam welded samples possess high values of both tensile and compressive stresses. For instance, Li et.al. [31] reported on the formation of high tensile residual stresses in the  $Ti_2AlNb$  alloy which can reach 1000 MPa in the fusion zone and its adjacent area. However, in wide weld seams their reduction is observed. Residual stresses also can be significantly reduced by varying the electron beam welding regimes or by applying modified welding techniques which allows decreasing the cooling rates and prolonging the high temperature stage. For instance, application of such method allowed to reduce stresses accumulated in  $\gamma$ -TiAl-based alloys to about 225 MPa [32]. This stress level does not provoke cracking in the welded zone. It should be noticed that no cracking was observed in clad layers obtained in the current study which means that a residual stress level was not extremely high. Probably, the reason for that consists in a heat distribution on a large surface area compared to a narrow electron beam exposure zone which forms at the electron beam welding process.

Nevertheless, X-ray tomography revealed some kind of defects in the coatings (Fig. 3). The  $\mu$ CT dataset was analyzed for pores and inclusions using VGStudio MAX 3.2. The analysis revealed that a density of voids was about 100 pores per  $1\text{ cm}^3$  and amount of inclusions was about 30 in  $1\text{ cm}^3$  of a coating. Figure 3a displays a 3D rendering of the detected pores and inclusions. The size distribution of the pores and inclusions is show in Fig. 3b. The inclusions are all spherical, smaller than  $100\text{ }\mu\text{m}$  in diameter with a mean size of  $70\text{ }\mu\text{m}$ , and of approximately 80 % higher density than the surrounding material. This can be the evidence of the presence of unmelted high-dense Nb particles. The average pore diameter is  $190\text{ }\mu\text{m}$ .

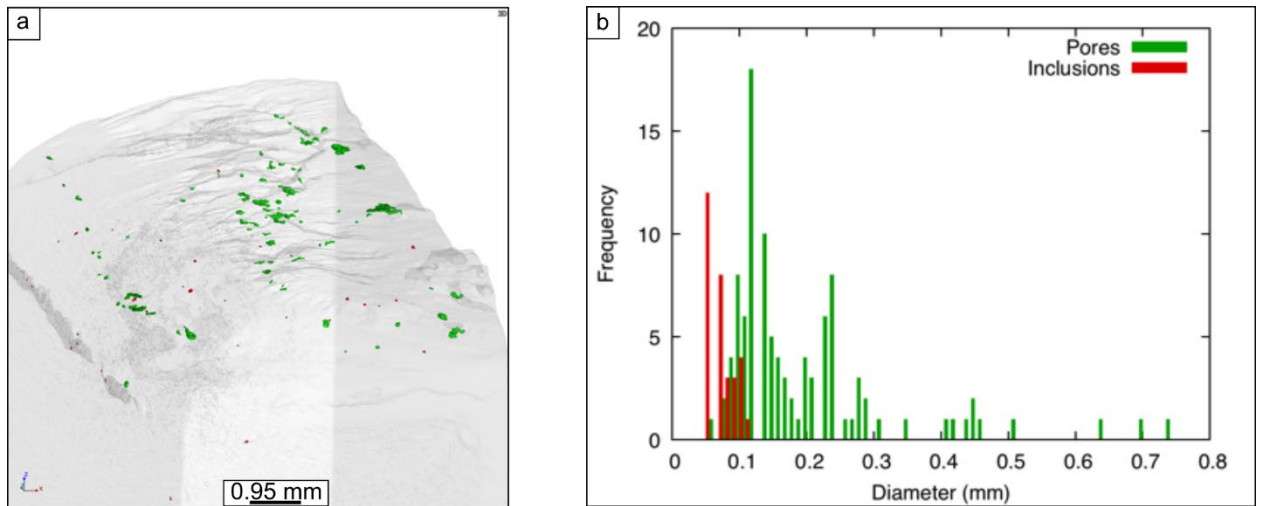


Fig. 3. Results of X-ray tomography of the Ti-46Al-8Nb sample: a - 3D rendering of the distribution of pores (green) and inclusions (red) in the test piece; b - size distribution of the pores (green) and inclusions (red).

Investigation of the structure and chemical composition of the coatings was performed using a combination of SEM and EDX. The structure of the alloyed layers is shown in Fig. 4 and the compositions determined by single point and area measurements within the microstructure are given in Table 2. This table also contains information on the probable phases present at the different measurement positions within the microstructure based on the EDX analysis, determined using additional information from the Ti-Al-Nb phase diagram and actual phase compositions determined from the X-ray diffraction results.

A distinct macrostructural particularity of the coatings is that the inhomogeneity of the coatings increases with increasing Nb and decreasing Al content. The dendritic structure with a non-uniform distribution of elements between the dendrite branches and the interdendritic regions was the characteristic of all cladded layers. For example, in the interdendritic regions of the Ti-48Al-2Nb coating, the Al concentration was slightly higher (Fig. 4a, Table 2, point 4) than that in the branches. It is clearly seen at higher magnifications, that dendrite branches consist of fine needles (Fig. 4a, area 2). Besides dendrites, the presence of a lamellar-like structure was observed in the form of large uniform areas within the cladded layer (Fig. 4a, Table 2, area 1). On average, the needles found in dendritic areas (Table 2, area 2) contain a higher amount of Al compared to large lamellar-like zones, where the Al is below 37 at. % (Table 2, area 1).

The average composition of the Ti-48Al-2Nb cladding layer obtained in our study is Ti-43.6Al-1.2Nb. Thus, the content of alloying elements (Al and Nb) in this coating was slightly lower than was expected due to the partial loss of alloying powder during the electron beam processing. At the same time, dilution of alloying powders with the melted substrate material keeps the titanium content at a high level.

The Ti-46Al-8Nb and Ti-43Al-14Nb coatings mainly have a dendritic structure. Needle-like areas form in these samples as isolated “islands” and have a reduced Al content compared to dendritic zones. In fact, the average composition in Ti-46Al-8Nb and Ti-43Al-14Nb cladded layers was: Ti-49.9Al-6.2Nb and Ti-45.7Al-11.6Nb respectively. The coating with the highest Nb content also contained a slightly higher amount of Al than expected. This effect is probably related to the depth of the electron beam penetration in the material. As mentioned above, the maximum electron energy release was located closer to the surface in the coating that had a higher Nb concentration. Thus, the melting depth of base material with a high Nb containing coating decreases and consequently the dilution of the coating material with titanium from the substrate also decreases. Moreover, in the Ti-40Al-20Nb coating, areas with elevated Nb content

(up to 70 at. %) were observed, which possibly indicates that a higher energy input is required to obtain a uniform cladded layer. The actual composition of the sample was Ti-41.7Al-16.3Nb.

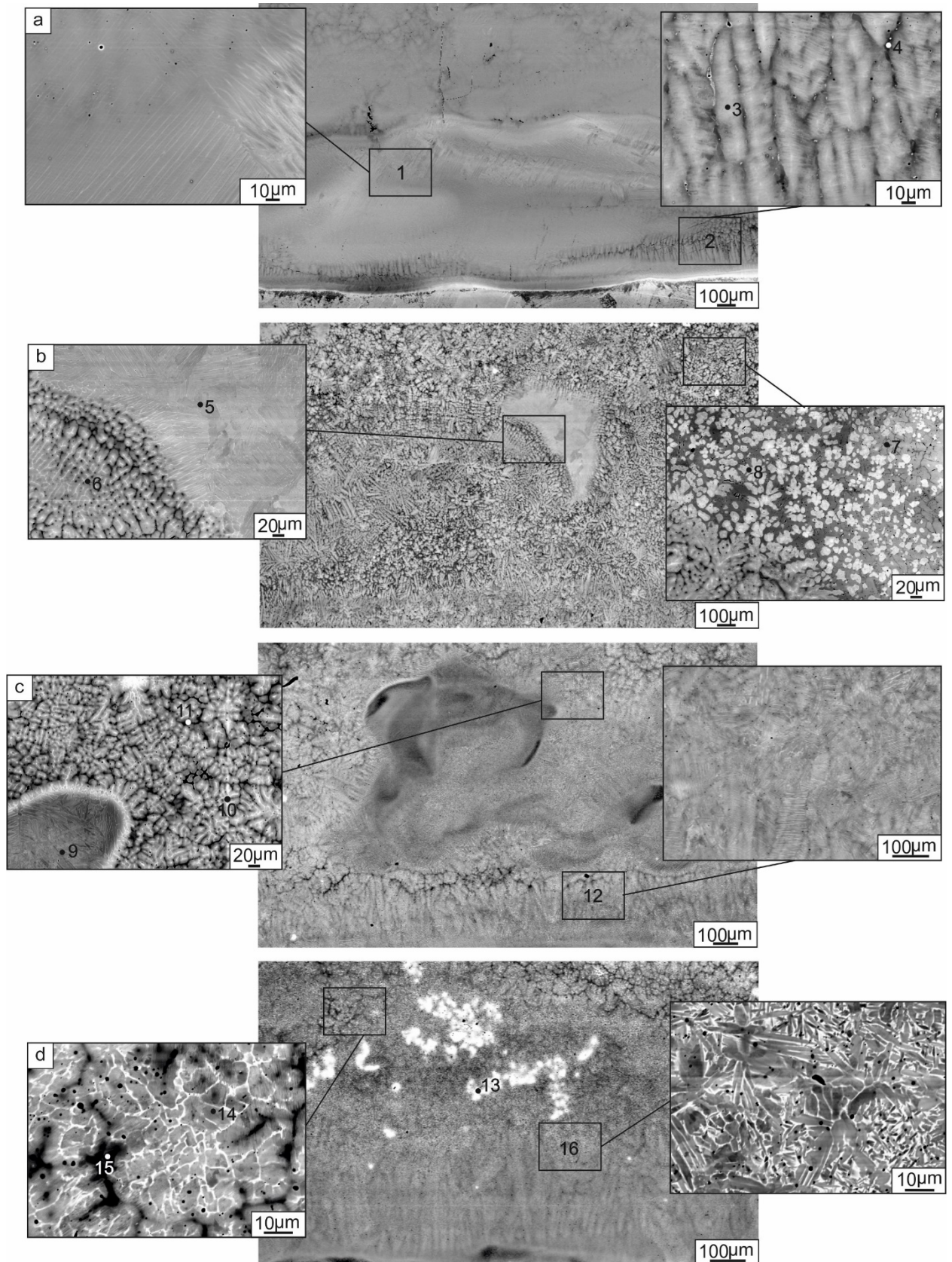


Fig. 4. Microstructure of the obtained coatings: a - Ti-48Al-2Nb; b - Ti-46Al-8Nb; c - Ti-43Al-14Nb; d - Ti-40Al-20Nb. Separate areas in the pictures pointed with numbers from 1 to 16 correspond to points of EDS analysis summarized in Table 2.

Table 2. Results of the elemental analysis of clad layers (in at. %). Analysis was carried out in both local areas shown in Fig. 4 and over the entire thickness. The compositions determined from measurement over the entire thickness are given as the “mean value” in Table.

	Ti	Al	Nb	Ta	Assumed phases (based on Ti-Al-Nb phase diagram)* [33]	Actual phases determined from X- ray diffraction
Ti-48Al-2Nb						
Mean value	55.2	43.6	1.2	-		$\alpha_2$
1	61.7	37.3	1.0		$\alpha_2+\gamma$	
2	45.8	52.7	1.5		$\gamma$	
3	48.9	49.6	1.4		$\gamma$	
4	44.4	54.6	1.0		$\gamma$	
Ti-46Al-8Nb						
Mean value	43.8	49.9	6.2			$\alpha_2+\omega(\beta)+\alpha$
5	49.4	44.8	5.8		$\gamma+\omega$	
6	46.8	47.4	5.8		$\gamma+\omega$	
7	33.2	58.3	8.5		$\gamma+\omega$	
8	41.2	50.6	8.1		$\gamma$	
Ti-43Al-14Nb						
Mean value	42.8	45.6	11.6			$\alpha_2+\omega(\beta)$
9	53.5	37.0	9.5		$\alpha_2+\gamma+\omega$	
10	34.8	53.2	12.1		$\gamma+\varepsilon$	
11	35.9	49.0	15.1		$\gamma+\omega$	
12	46.7	42.8	10.5		$\gamma+\omega$	
Ti-40Al-20Nb						
Mean value	41.7	42.0	16.3			$\alpha_2+Al_3Ti+\gamma_1+\alpha$
13	4.3	25.8	69.9		$\sigma+\delta$	
14	40.3	33.8	25.7	0.2	$\omega+O+\sigma$	
15	27.2	55.5	17.3		$\gamma+\varepsilon$	
16	33.0	47.0	20.1		$\gamma+\tau+\sigma$	

\* To establish the relationship between the measured composition and phases, an isothermical section of Ti-Al-Nb phase diagram at 700 °C (the minimum temperature available for the full ternary diagram) was used.

Based on the elemental analysis of local microvolumes it is possible to deduce which phases should be present at that location by comparing with the ternary Ti-Al-Nb phase diagram. The comparison results are shown in Table 2. For coatings with a low Nb content (up to 2 at. %), the only phases found in the binary Ti-Al system are expected. The Al to Ti ratio in different regions of the Ti-48Al-2Nb coating is typical for the presence of two phases, namely TiAl and Ti<sub>3</sub>Al [2]. It was mentioned in [34] that small additions of transition metals were dissolved in TiAl and Ti<sub>3</sub>Al phases and mostly substituted for Ti atoms. Diao et. al [35] have also shown that Nb can substitute for Al atoms in TiAl at some Ti:Al ratios. Increasing the Nb content results in the formation of additional phases. Being a  $\beta$ -stabilizer, Nb contributes to the formation  $\beta$ (B2)-phase. By further increasing the Nb content, one can obtain different ternary phases, such as  $\omega$ -phase with a hexagonal lattice, O-phase corresponding to Ti<sub>2</sub>NbAl and others. However,

identification of phases on the basis of elemental analysis is an unreliable approach. Thus, in this study X-ray diffraction was used to analyze the phases within the coatings.

### 3.1.2. Phase analysis of the coatings

The results of X-ray diffraction analysis are given in Fig. 5. It was found that the actual phase composition was different from that of predicted by phase diagram or that which normally can be found in cast alloys. According to Ding et al. [36] the following distribution of phases occurs in cast Ti-Al-Nb alloys: dendrite branches containing predominantly  $\alpha_2$ -phase, separated by interdendritic space consisting of  $\gamma$ -TiAl. In present study, Ti-48Al-2Nb sample consisted of only one phase namely  $\alpha_2$ -Ti<sub>3</sub>Al.

In the Ti-46Al-8Nb coating, besides  $\alpha_2$ -Ti<sub>3</sub>Al, the  $\alpha$ -Ti and  $\omega$ -phases were also found. Authors of [36] mention that in high niobium containing alloys (about 8 at. % Nb) light thin ridges corresponding to  $\beta$ -phase, precipitate in the central parts of the dendrite branches appear. However, according to Song et. al [37],  $\beta$ (B2) represents a matrix phase, in which particles of  $\omega$  precipitate. A mechanism of  $\beta$ (B2) formation and its transformation to  $\omega$  in high-Nb alloys was described in detail in [37, 38]. During solidification, residual  $\beta$ -phase containing an increased amount of Nb accumulates in the central part of dendrites and at triple junctions of grain boundaries. Later, the ordering of  $\beta$ -phase takes place in these areas and the B2 structure forms. These B2 grains consist of  $\omega$  particles distributed in a B2 matrix. The  $\omega$  particles form via heterogeneous nucleation at B2/ $\gamma$  grain boundaries or by homogeneous nucleation in the B2 matrix.

Peaks found in XRD patterns of the Ti-46Al-8Nb and Ti-43Al-14Nb coatings correspond to  $\omega$ -phase, however, the presence of  $\beta$ (B2) cannot be reliably identified from the analysis of these patterns. The reflections corresponding to  $\beta$ -phase should appear at  $2\theta \approx 3.12^\circ$ ,  $2\theta \approx 4.42^\circ$  and  $2\theta \approx 5.91^\circ$ , but these reflections fully overlap with  $\omega$ -phase peaks. The phases identified in the Ti-46Al-8Nb and Ti-43Al-14Nb samples are identical except that the latter alloy does not contain any  $\alpha$ -Ti.

$\gamma_1$ -Ti<sub>4</sub>Nb<sub>3</sub>Al<sub>9</sub> was the predominant phase in the Ti-40Al-20Nb sample. This phase has a tetragonal lattice ( $a=0.558$ - $0.584$  nm and  $c=0.815$ - $0.845$  nm) corresponding to a P4/mmm space group. Its formation occurs by ordering of Nb atoms in the  $\gamma$ -phase lattice [39]. In the equilibrium state,  $\gamma_1$  forms as needles along the [001] direction [40]. Both phases ( $\gamma$  and  $\gamma_1$ ) have a negative formation energy, however, formation energy of the  $\gamma$ -phase is lower ( $-0,449$  eV/at.) than that of  $\gamma_1$  ( $-0,369$  eV/at.). According to this, one can conclude that both phases are stable, however the formation of  $\gamma$ -phase is favored.  $\gamma_1$  however can be formed in non-equilibrium conditions. The Al<sub>3</sub>Ti in this coating probably originated from the inhomogeneous distribution of alloying elements.

Generally, the phase compositions of coatings obtained were different from the expected. Along with the formation of a range of metastable phases, such as  $\gamma_1$ , the other non-equilibrium phase transformations took place. The one example is absence  $\gamma$ -TiAl in the coatings. Kenel and Leinenbach [41] reported that the  $\alpha \rightarrow \alpha_2$  transformation instead of  $\alpha \rightarrow \gamma$  can often be observed after rapid cooling of ternary Ti-Al-Nb alloys. It was mentioned that for nucleation of the  $\gamma$ -phase a slight overcooling below  $T_0$  (corresponding to  $\alpha \rightarrow \gamma$ ) is necessary. However, if the  $\alpha \rightarrow \alpha_2$  point will be reached, an alloy can be subjected to  $\alpha_2$  ordering without the formation of  $\gamma$ -phase. This phenomenon can happen at cooling rates above  $4.4 \times 10^3$  K/s.

The other example of metastable processes is the appearance of  $\alpha$ -Ti reflections in the XRD patterns of Ti-46Al-8Nb and Ti-40Al-20Nb coatings. Let us consider two possible reasons of their occurrence. Firstly,  $\alpha$ -Ti peaks could appear as a result of irradiation from the substrate material. Although the coatings were cut away from the underlying titanium substrate before XRD analysis, nevertheless a small amount of substrate could remain within the investigated samples. Indeed, due to the inhomogeneity of the clad layers and the different depths of

remelting, a precise separation of the coating from the substrate is difficult. A second reason for the presence of  $\alpha$ -Ti peaks could result from the rapid cooling of the surface layer from the molten state. For instance, Kartavykh [42] reported that  $\alpha$ -Ti and  $\beta$ -Ti are the first phases that nucleate during solidification of a melt consisting of Al and Ti. It could be supposed in the present case that due to rapid cooling; the primary structure is retained in the coatings. Only at slow cooling rate (20 K/s) the primary phases decompose to  $\alpha_2+\gamma$  lamellae [42]. Thus, if we exclude presence of the  $\alpha$ -Ti peaks as arising from the substrate, one can conclude that cooling rates in our case were significantly higher than 20 K/s.

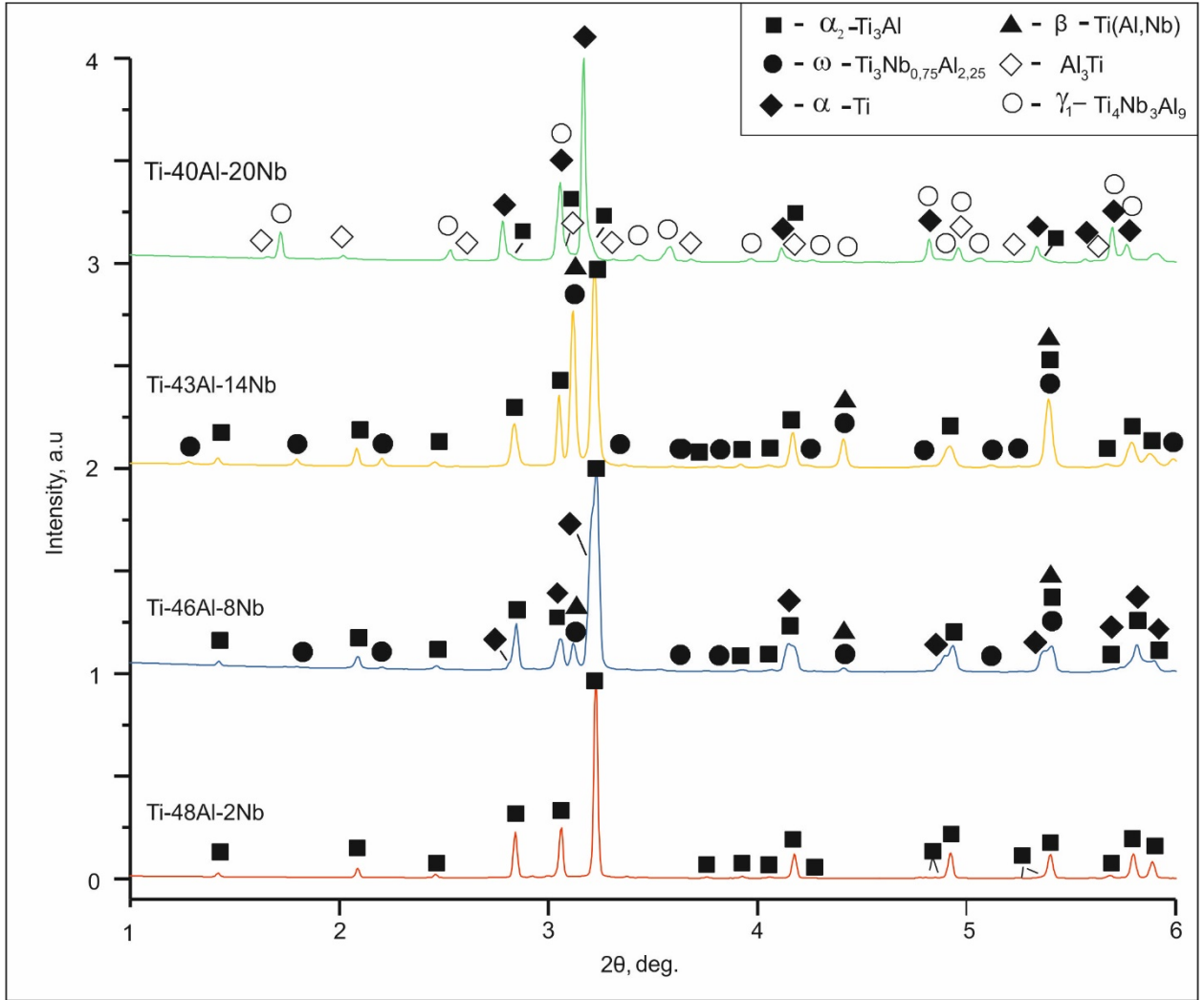


Fig. 5. Results of diffraction analysis of the coatings obtained by the electron beam treatment. The highest peak intensity was 3000 arbitrary units.

Thus, to explain metastable phase transformations such as disordering of  $\alpha_2$  resulted in  $\alpha$  occurrence as well as suppression of the  $\alpha \rightarrow \gamma$  and formation of  $\gamma_1$ , it is important to determine the range of cooling rates experienced by specimens in the present work. An estimation of the cooling rates was obtained as follows. For the sake of simplicity, it is assumed that heat transfer is regulated by the heat conductivity through the cladded layer into the substrate. Considering that heat predominantly dissipates in the direction perpendicular to a cladded layer, one can assume the cooling situation to be a one-dimensional problem. In this case the heat conductivity equation can be written as:

$$\frac{\partial T}{\partial t} = \alpha \frac{\partial^2 T}{\partial x^2} \quad (3)$$

where  $T=T(x,t)$  is a function that describes the change of temperature and depends on time ( $t$ ) and distance ( $x$ ) from the upper to the lower surface of the sample;  $\alpha$  is a thermal diffusivity coefficient.

Assuming that a convective heat exchange with the environment occurs at the boundaries of the computational domain and taking the average values of the thermophysical properties of the material, this equation can be easily solved by using the finite difference method. The choice of initial conditions has been made as follows. Since the electron beam processing regimes have been chosen so that most of the electron energy is released into the cladded layer, it can be roughly assumed that the substrate practically does not heat up and its temperature is approximately equal to the ambient temperature. At the same time, the temperature reached in the deposited layer exceeds the melting point of niobium.

The results of this analysis under the above mentioned assumptions, are shown in Fig. 6. Figure 6a shows the temperature change over time in the middle of the cladded layer, and Fig. 6b represents the cooling rate.

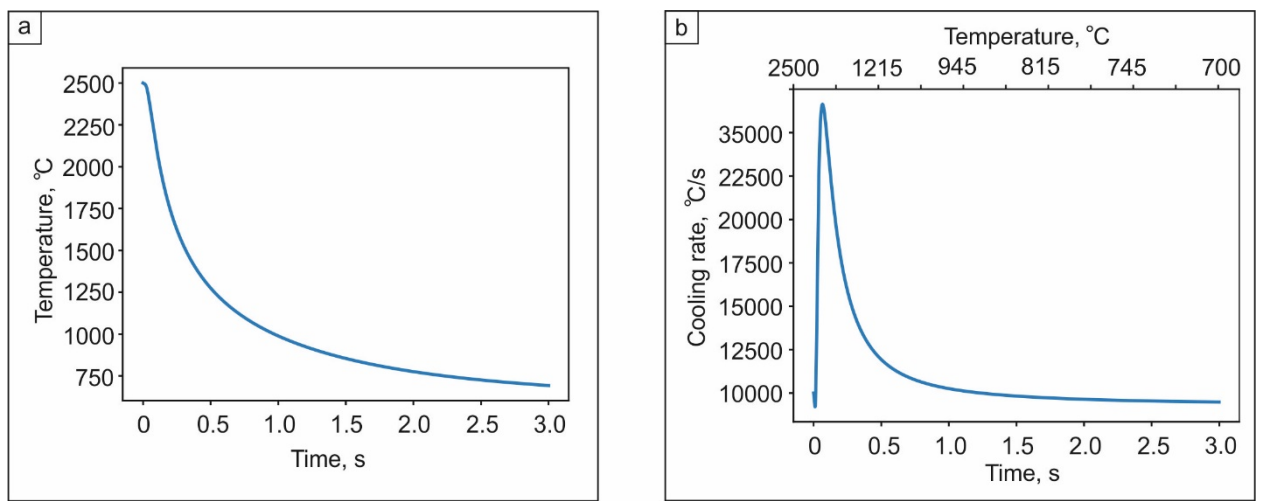


Fig. 6. Changes in the temperature (a) and cooling rates (b) in the middle part of a cladded layer after ending the electron beam exposure.

At the first moment of time the temperature gradient in the middle of the cladded layer is low (provided that it was heated with the electron beam relatively uniformly), thus the cooling rate is also relatively low. As the temperature gradient increases due to the rapid heat transfer from the coating to the substrate, the cooling rate reaches a peak value of several tens of thousands of °C/s. After that the cooling rate starts decreasing since the temperature equalizes and the temperature gradient decreases again. It may be noticed, that radiation heat transfer from the upper interface was neglected in the calculation. Thus, the actual cooling rate may be even higher during initial moments of cooling.

The metastable phases, which are considered in the current study are formed as a result of phase transformations occurring in a solid state, thus the cooling rate of material when it is solid is of great importance. As follows from the calculations the cooling rate at temperatures below the melting point may be as high as  $10^4$  °C/s. The obtained value is in good agreement with the results obtained by Ivanov et.al [43] and Skeebe et al. [44], who analyzed the electron-beam surface treatment more thoroughly. Thus, despite a number of assumptions being made in our calculations, it can be concluded that the cooling rate after the electron beam cladding is quite high and comparable to the cooling rates that occur during rapid quenching of metals.

### 3.1.3. Investigating the fine structure of the cladded layers

For a more detailed identification of the structures and phases formed in the coatings, TEM investigations were performed. Studying the fine structure established that the predominant phase ( $\text{Ti}_3\text{Al}$ ) formed as grains containing antiphase boundaries (Fig. 7a-c). The main condition for the formation of antiphase boundaries is rapid quenching from temperatures above 1300 °C which promotes ordering of the structure. The cladded layers experience such rapid cooling and thus the appearance of antiphase boundaries is a natural consequence of the processes occurring during coating manufacture. TEM investigations also confirmed the existence of  $\alpha$ -Ti in the cladded layers. Analysis of the fine structure of the Ti-46Al-8Nb sample revealed that along with  $\alpha_2$ ,  $\alpha$ -phase was found in local areas (Fig. 7d-f).

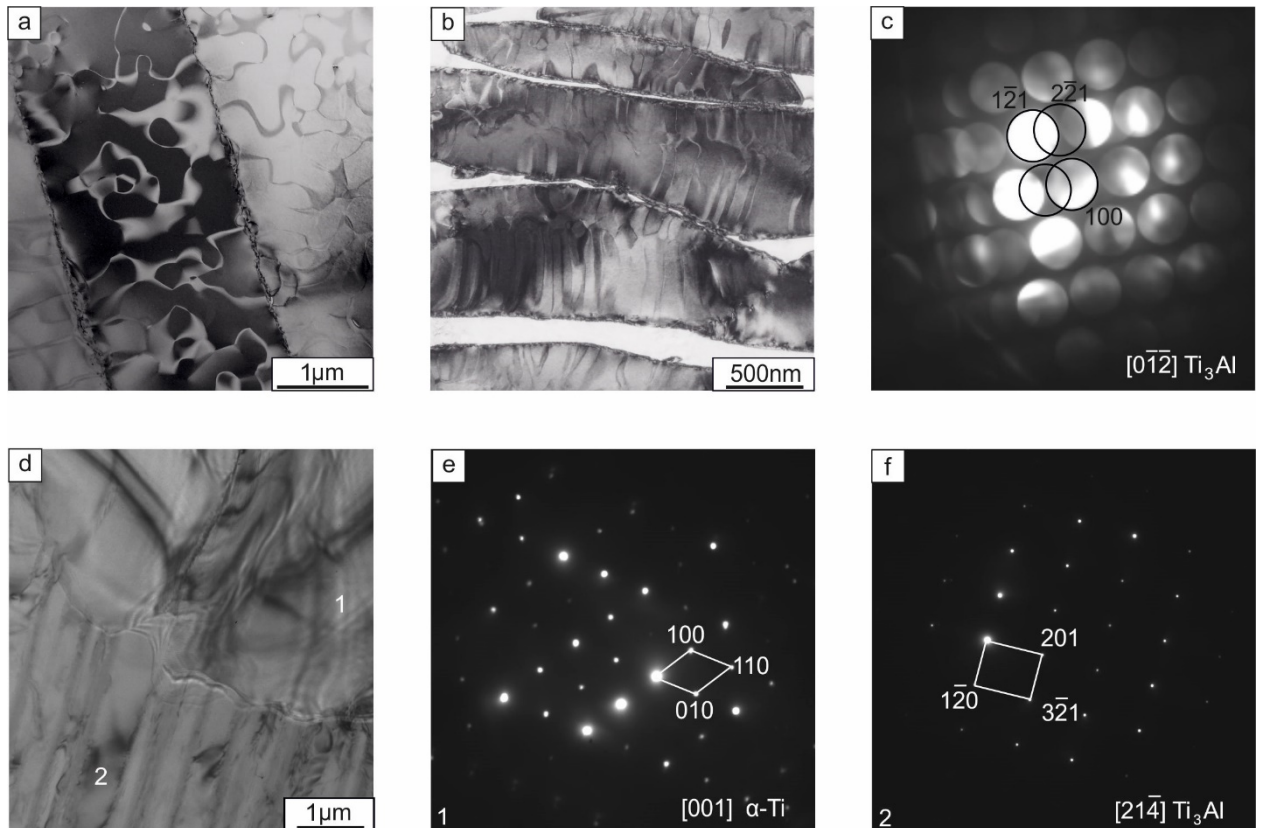


Fig. 7. Fine structure of the coatings - a, b: Ti-48Al-2Nb, d: Ti-46Al-8Nb; and electron diffractions obtained from different areas of the samples - c: Ti-48Al-2Nb, e-f: Ti-46Al-8Nb.

Another aspect consisted in identification of the  $\omega$ -phase which has peaks that coincide with  $\beta$ -Ti reflections in XRD pattern. Electron diffraction analysis showed that the  $\omega$ -phase precipitated in coatings as separate grains that neighbor  $\text{Ti}_3\text{Al}$  grains. In some cases (as is shown in Fig. 8a,c) it was not possible to reliably identify the  $\omega$ -phase, because for some grain orientations the measured angles and interplanar distances correspond to both  $\beta$ - and  $\omega$ -phase. However, for the orientation shown in Fig. 8e, the  $\omega$ -phase can be reliably identified. It is also necessary to note a particularity observed while analyzing this electron diffraction pattern. A row of reflections ((021), (011), (001) etc.) which, according to the simulation shown in Fig. 8f is characterized by low intensities at full ordering of  $\omega$ -phase, was not found in the diffraction pattern shown in Fig. 8e. This image corresponds to metastable  $\omega'$ -phase, an intermediate phase in the  $\beta(\text{B2}) \rightarrow \omega$  transformation.  $\omega'$  forms by a diffusionless transition of B2 and has a P-3m1 space group with four different Wyckoff positions (1a, 1b, 2d<sub>1</sub> and 2d<sub>2</sub>), however, only two of them are occupied (1a and 1b positions that are occupied by atoms in the B2 structure) [38].



role. For example, samples produced by powder metallurgy possessed the hardness of about 350 HV [47]. In our case the microhardness was higher than that of the alloys produced by other techniques. This could be related to the high cooling rates promoting formation of finer microstructure with higher inhomogeneous lattice strains.

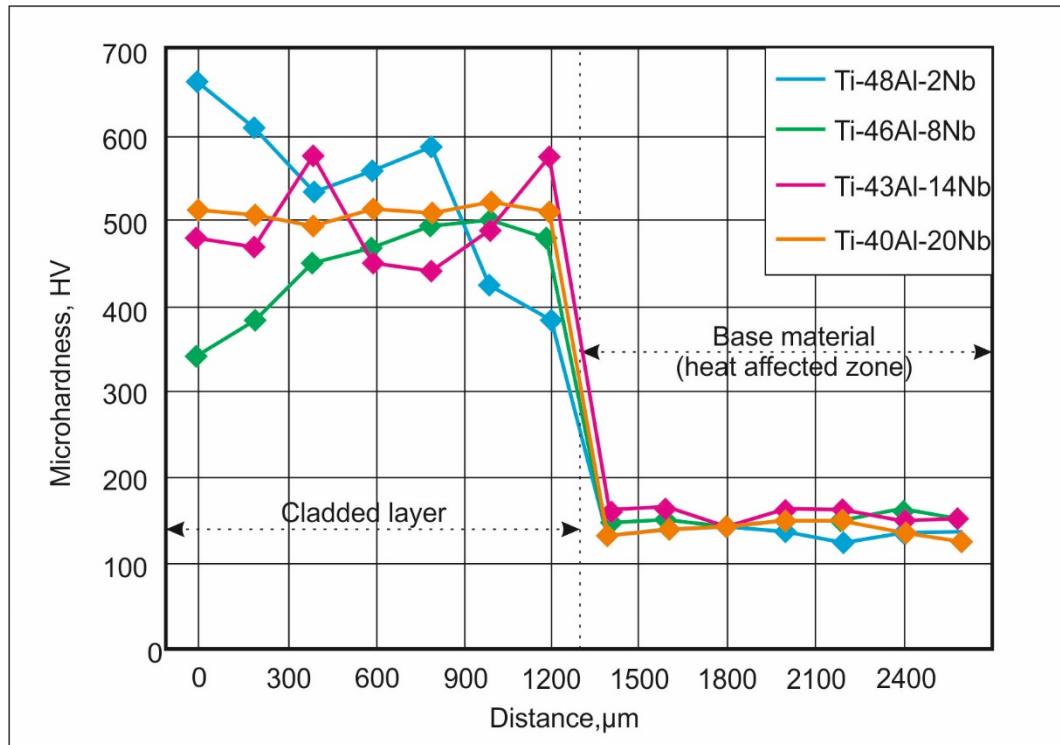


Fig. 9. Results of microhardness measurements.

As a general rule, increasing microhardness leads to improved tribological properties and in particularly wear resistance. To determine the room temperature wear resistance, friction tests were made against fixed abrasive particles. Results of the tests are shown in Fig. 10.

The maximum improvement of wear resistance compared to the reference sample (the Ti-base material) was observed for the Ti-48Al-2Nb and Ti-40Al-20Nb coatings, the relative wear resistance being 1.75 times higher. The data obtained correlates well with the results of the microhardness measurements. A possible reason for the low wear resistance of the Ti-46Al-8Nb and Ti-43Al-14Nb cladded layers is the presence of  $\beta/\omega$ -phase which is characterized by a low microhardness (about 220-250 HV) [48] relative to other intermetallic phases formed in the Ti-48Al-2Nb and Ti-40Al-20Nb coatings. The lowest wear resistance was determined for the Ti-43Al-14Nb cladded layer, which was characterized by the most intensive  $\beta/\omega$ -phases XRD peaks among the different coatings. According to a brief Rietveld analysis performed by means of MAUD [49], the volume fraction of  $\beta/\omega$  in this coating reached a value of approximately 30 %. However, one can expect that the wear resistance of the cladded layers (independently on their composition) will be higher than that of the cast Ti-48Al alloy due to the higher hardness.

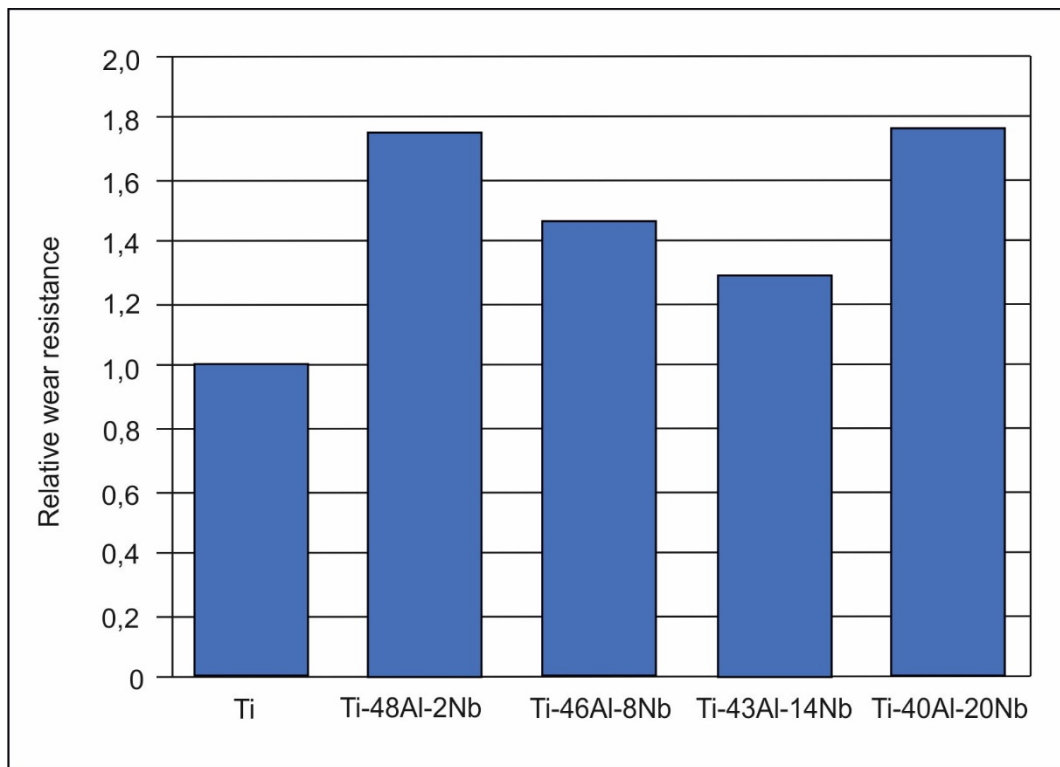


Fig. 10. Results of the friction tests against alundum grit.

To evaluate the behavior of the coatings under high-temperature conditions, creep and oxidation tests were performed. Cyclic oxidation of the clad layers showed that all coatings had a superior oxidation resistance compared to the Ti-substrate material (Fig. 11). The Ti-48Al-2Nb, Ti-46Al-8Nb and Ti-43Al-14Nb samples all had a mass gain of less than 1 mg/cm<sup>2</sup> after holding for 200 hours at 900 °C. It is well-recognized fact that the minor Nb additions (about 2 %) to structural ( $\gamma+\alpha_2$ ) intermetallic alloys significantly increase their oxidation resistance due to the following reasons: reduced growth rate of an oxide film at high temperatures, good adhesion between an oxide scale and a substrate, low dissolution of oxygen in intermetallic layer neighboring with an oxide scale and the growth of homogeneous titanium-rich nitride zone in this area, the absence of an Al-depleted zone below the oxide scale [50]. However, information about influence of a higher Nb content is still quite contradictory. While some studies declaim that small additions are enough to provide the best oxidation resistance [51-53], it was reported in other publications that increase of Nb content can further improve the aforementioned characteristic [54, 55]. Particularly, in study [50] it was shown, that alloying of titanium aluminide alloys with 8.5 at. % Nb is beneficial. Our experiments also showed that addition of about 8 at. % Nb gives the best oxidation resistance. The positive effect of a higher amount of Nb (in the vicinity to 10 at. %) can be attributed to enhanced formation of external alumina scale [55].

Oxidation of the Ti-40Al-20Nb coating was more significant than the other samples; the mass gain of this sample after 200 hours at 900 °C was 3 mg/cm<sup>2</sup>. A possible reason for the reduced oxidation resistance of this coating may be its low Al content. Moreover, EDX analysis revealed an extremely inhomogeneous distribution of alloying elements across the coating (see Table 2) and the presence of highly depleted Al zones. It is well-known [56] that oxidation resistance of Ti-Al-based alloys improves with increasing Al content due to the ability of Al to form an Al<sub>2</sub>O<sub>3</sub> protective oxide layer on the surface of oxidized specimens. Thus, in the areas containing less than 5 at. % Al, the formation of titanium oxide is expected and would lead to a large weight gain.

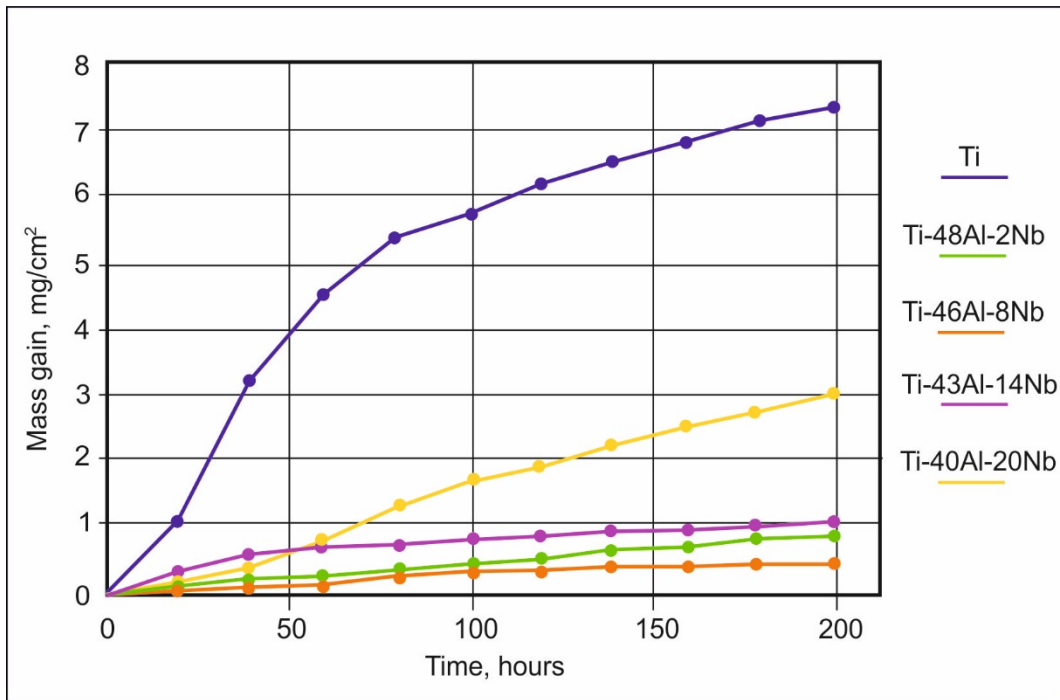


Fig. 11. Mass gain curves of the samples subjected to cyclic oxidation at 900 °C.

The phases present in the oxide scales formed after oxidation for 200 hours at 900 °C were analyzed using XRD in a laboratory diffractometer (Fig. 12). The oxide scales formed at the surfaces of the most resistant samples (Ti-48Al-2Nb, Ti-46Al-8Nb and Ti-43Al-14Nb) had similar phases: Al<sub>2</sub>O<sub>3</sub> and rutile (TiO<sub>2</sub>). Investigation of the oxides on the surface of the Ti-40Al-20Nb sample showed that besides the two aforementioned oxides, the AlNbO<sub>4</sub> phase with a monoclinic lattice had also formed. As mentioned in [57, 58], the formation of such a phase results in an increase of the oxidation rate.

It is well-known that the creep resistance of titanium aluminides depends on many factors, such as the type of microstructure, impurities, processing way etc. For example, creep rate of Ti-48Al at nearly the same testing conditions as applied in our study can vary in the range from about  $5 \times 10^{-5} \text{ s}^{-1}$  to  $10^{-7} \text{ s}^{-1}$  [59, 60]. The lowest value was observed for equiaxed microstructure [60]. Lamellar microstructure demonstrates the value of  $10^{-6} \text{ s}^{-1}$ , however refinement of lamellas allows decreasing creep rate to  $10^{-7} \text{ s}^{-1}$  [60-62]. Creep rate of typical duplex microstructure is about  $10^{-7} \text{ s}^{-1}$  [62]. However, commercially important TiAl-based alloys as a rule contain alloying elements which improve mechanical and functional characteristics. Creep resistance of the alloys with additions of Nb, Cr, V, W etc. is usually in the same range as that of Ti-48Al and depends on the amount and types of alloying elements and heat treatment regimes [22, 63, 64]. Thus, the creep rate values of titanium aluminides with Nb additions obtained in our study were expected to be of the same order of magnitude as those reported in the literature. Indeed, compressive creep tests at a temperature of 800 °C under a 250 MPa load showed that all clad materials were characterized by a creep rate of  $10^{-6} - 10^{-7} \text{ s}^{-1}$  (Fig. 13). The Ti-40Al-20Nb coating demonstrated the lowest creep resistance. The secondary creep rate of this alloy was  $4.5 \times 10^{-6} \text{ s}^{-1}$ . The creep resistance increased with increasing Al content in the alloys. The lowest secondary creep rate ( $2.3 \times 10^{-7} \text{ s}^{-1}$ ) was for the Ti-48Al-2Nb coating.

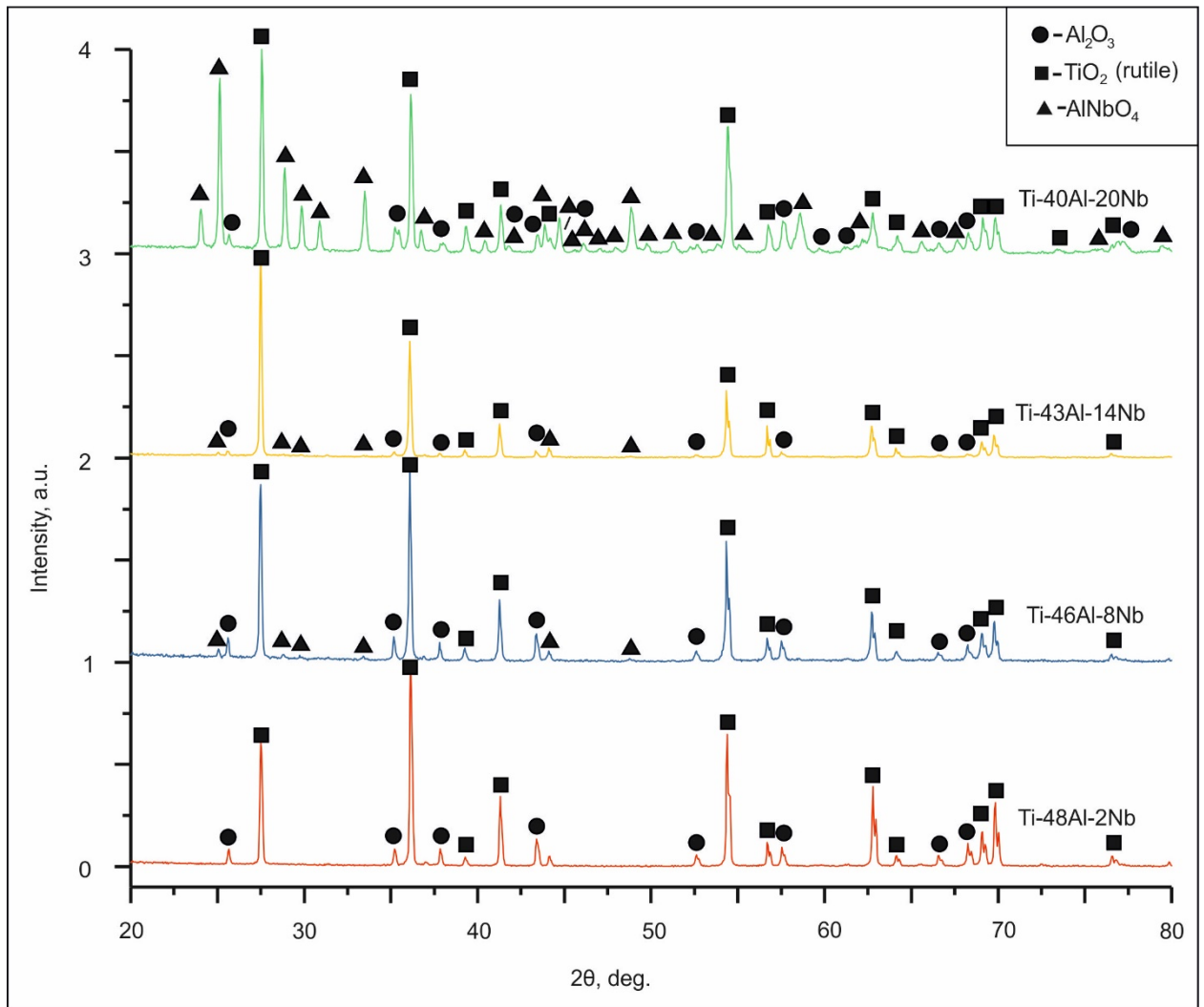


Fig. 12. Diffractograms after oxidation at 900 °C for 200 hours. The position of peaks relating to certain oxide phases are indicated. The highest peak intensity was 1500 counts per second.

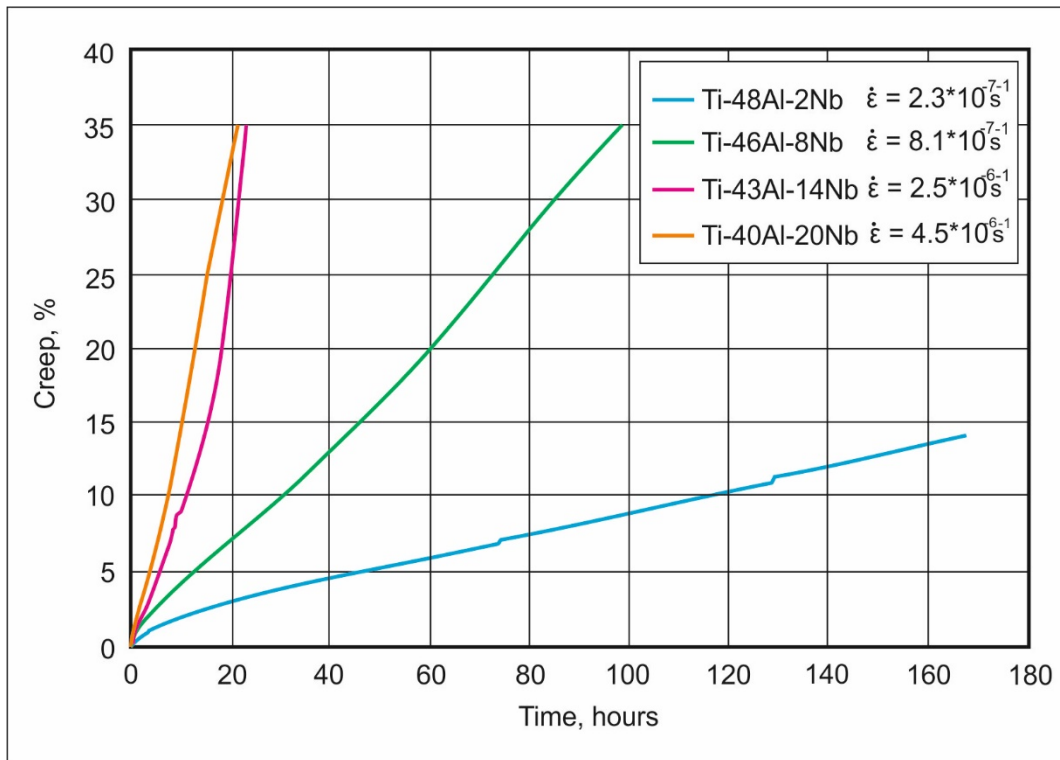


Fig. 13. Compressive creep curves of the cladded layer materials tested at 800 °C and under a load of 250 MPa.

### Conclusions

1. It was possible to obtain Ti-Al-Nb based coatings at the surfaces of titanium workpieces processed by non-vacuum electron beam treatment by adjusting the Nb and Al content. By this, the mechanical and other properties of the cp-Ti substrate can be modified.

2. The phases present in the coatings depend on the powder mixture placed above the Ti-substrate before electron beam processing. The  $\alpha_2$ -Ti<sub>3</sub>Al phase forms in all coatings independent of the Al and Nb concentration. Formation of the  $\gamma$ -phase is suppressed in these coatings and Al and Nb form a solid solution in the  $\alpha$ -Ti. In the alloy with 20 at. % Nb and 40 at. % Al a  $\gamma_1$ -phase was obtained. The  $\beta$ (B2)-phase in the cladded layers with 8 and 14 at. % Nb (containing 46 and 43 at. % Al respectively) transformed to  $\omega'$ -Ti (an intermediate phase that forms during the  $\beta$ (B2)→ $\omega$  transformation). Thus, the phases present in the coatings differ from those predicted from the phase diagram. The formation of metastable phases during the electron beam treatment most probably resulted from the extremely high cooling rates the cladded layers experienced after the treatment was terminated and the inhomogeneous distribution of alloying elements across the coatings.

3. Varying the Nb and Al concentration influenced the size of the heat affected zone. Low Al and high Nb contents increase the near surface energy loss and thus decrease the penetration depth of the electron beam and consequently the depth of the heat affected zone.

4. The highest hardness and wear resistance were shown by alloys that did not contain the  $\omega$ -phase (Ti-48Al-2Nb and Ti-40Al-20Nb). The high temperature creep and oxidation properties decreased proportionally with increasing Nb and decreasing Al content in the cladded layers.

### Acknowledgement

Funding for this research has been provided by the Alexander von Humboldt Foundation.

### Data availability

The raw/processed data required to reproduce these findings cannot be shared at this time as the data also forms part of an ongoing study

## References

- [1] G. Lütjering, J.C. Williams, Titanium, Springer Berlin Heidelberg New York, 2007.
- [2] Alloy Phase Diagrams, ASM Handbook, 1992.
- [3] C. Parlikar, M.Z. Alam, D.K. Das, Effect of AL3Ti diffusion aluminide coating on tensile properties of a near  $\alpha$ -Ti alloy, *Mat. Sci. Eng. A*, 530 (2011) 565-573.
- [4] J.L. Smialek, Oxidation behaviour of TiAl<sub>3</sub> coatings and alloys, *Corrosion Science*, 35 (1993).
- [5] M. Góral, A. Gradzik, J. Sieniawski, R. Filip, M. Wierzbinska, The influence of activator on vapour phase aluminizing of TiAl intermetallics, *Solid State Phenomena*, 2015, pp. 357-360.
- [6] Z.G. Zhang, Y.P. Peng, Y.L. Mao, C.M. Hou, L. Xu, Hot-dip aluminizing fabrication of TiAl<sub>3</sub> coating on TA15 alloy and its high temperature oxidation behaviors, *High Temperature Materials and Processes*, 30 (2012) 519-525.
- [7] Z.G. Zhang, Y.P. Peng, Y.L. Mao, C.J. Pang, L.Y. Lu, Effect of hot-dip aluminizing on the oxidation resistance of Ti-6Al-4V alloy at high temperatures, *Corrosion Science*, 55 (2012) 187-193.
- [8] T. Sasaki, T. Yagi, T. Watanabe, A. Yanagisawa, Aluminizing of TiAl-based alloy using thermal spray coating, *Surface and Coatings Technology*, 205 (2011) 3900-3904.
- [9] M. Goral, G. Moskal, L. Swadzba, Gas phase aluminizing of TiAl intermetallics, *Intermetallics*, 17 (2009) 669-671.
- [10] Z.G. Zhang, X. Teng, Y.L. Mao, C.X. Cao, S.J. Wang, L. Wang, Improvement of oxidation resistance of  $\gamma$ -TiAl at 900 and 1000 °C through hot-dip aluminizing, *Oxidation of Metals*, 73 (2010) 455-466.
- [11] B. Guo, J. Zhou, S. Zhang, H. Zhou, Y. Pu, J. Chen, Phase composition and tribological properties of Ti-Al coatings produced on pure Ti by laser cladding, *Applied Surface Science*, 253 (2007) 9301-9310.
- [12] B. Guo, J. Zhou, S. Zhang, H. Zhou, Y. Pu, J. Chen, Tribological properties of titanium aluminides coatings produced on pure Ti by laser surface alloying, *Surface and Coatings Technology*, 202 (2008) 4121-4129.
- [13] S. Mridha, H.S. Ong, L.S. Poh, P. Cheang, Intermetallic coatings produced by TIG surface melting, *Journal of Materials Processing Technology*, 113 (2001) 516-520.
- [14] T. Matsubara, T. Shibutani, K. Uenishi, K.F. Kobayashi, Fabrication of a thick surface layer of Al<sub>3</sub>Ti on Ti substrate by reactive-pulsed electric current sintering, *Intermetallics*, 8 (2000) 815-822.
- [15] J. Cizek, O. Man, P. Roupčova, K. Loke, I. Dlouhy, Oxidation performance of cold spray Ti-Al barrier coated  $\gamma$ -TiAl intermetallic substrates, *Surface and Coatings Technology*, 268 (2015) 85-89.
- [16] B. Cárcel, A. Serrano, J. Zambrano, V. Amigó, A.C. Cárcel, Laser cladding of TiAl intermetallic alloy on Ti6Al4V. Process optimization and properties, *Physics Procedia*, 2014, pp. 284-293.
- [17] C. Guo, J. Zhou, J. Zhao, L. Wang, Y. Yu, J. Chen, H. Zhou, Improvement of the oxidation and wear resistance of pure Ti by laser-cladding Ti 3Al coating at elevated temperature, *Tribology Letters*, 42 (2011) 151-159.
- [18] I.N. Maliutina, H. Si-Mohand, J. Sijobert, P. Bertrand, D.V. Lazurenko, I.A. Bataev, Structure and oxidation behavior of  $\gamma$ -TiAl coating produced by laser cladding on titanium alloy, *Surface and Coatings Technology*, 319 (2017) 136-144.
- [19] I.A. Bataev, D.V. Lazurenko, M.G. Golkovsky, I.S. Laptev, I.K. Chakin, I.S. Ivanchik, Surface alloying of titanium with aluminium by non-vacuum electron beam cladding of powder mixtures, *Obrabotka metallov: metal working and material science*, 1 (2017) 51-60.

- [20] D.V. Lazurenko, I.A. Bataev, I.S. Laptev, A.A. Ruktuev, I.N. Maliutina, M.G. Golkovsky, A.A. Bataev, Formation of Ti-Al intermetallics on a surface of titanium by non-vacuum electron beam treatment, *Materials Characterization*, 134 (2017) 202-212.
- [21] M.G. Golkovski, I.A. Bataev, A.A. Bataev, A.A. Ruktuev, T.V. Zhuravina, N.K. Kuksanov, R.A. Salimov, V.A. Bataev, Atmospheric electron-beam surface alloying of titanium with tantalum, *Mat. Sci. Eng. A*, 578 (2013) 310-317.
- [22] F. Appel, J.D.H. Paul, M. Oehring, *Gamma Titanium Aluminide Alloys*, Wiley-VCH Verlag GmbH&Co. KGaA, Weinheim, 2011.
- [23] L.A. Feldkamp, L.C. Davis, J.W. Kress, Practical cone-beam algorithm, *Journal of the Optical Society of America A: Optics and Image Science, and Vision*, 1 (1984) 612-619.
- [24] T. Tabata, R. Ito, An Algorithm for the Energy Deposition by Fast Electrons, *Nuclear Science and Engineering*, 53 (1974) 226-239.
- [25] G. Benghalia, J. Wood, Material and residual stress considerations associated with the autofrettage of weld clad components, *International Journal of Pressure Vessels and Piping*, 139-140 (2016) 146-158.
- [26] H. Köhler, K. Partes, J.R. Kornmeier, F. Vollertsen, Residual Stresses in Steel Specimens Induced by Laser Cladding and their Effect on Fatigue Strength, *Physics Procedia*, 2012, pp. 354-361.
- [27] J. Chen, S.H. Wang, L. Xue, On the development of microstructures and residual stresses during laser cladding and post-heat treatments, *Journal of Materials Science*, 47 (2012) 779-792.
- [28] A. Plati, J.C. Tan, I.O. Golosnoy, R. Persoons, K. Van Acker, T.W. Clyne, Residual stress generation during laser cladding of steel with a particulate metal matrix composite, *Advanced Engineering Materials*, 8 (2006) 619-624.
- [29] E. Tiferet, O. Rivin, M. Ganor, H. Ettetdgui, O. Ozeri, E.N. Caspi, O. Yeheskel, Structural investigation of selective laser melting and electron beam melting of Ti-6Al-4V using neutron diffraction, *Additive Manufacturing*, 10 (2016) 43-46.
- [30] T. Maimaitiyili, R. Woracek, M. Neikter, M. Boin, R.C. Wimpory, R. Pederson, M. Strobl, M. Drakopoulos, N. Schäfer, C. Bjerkén, Residual lattice strain and phase distribution in Ti-6Al-4V produced by electron beam melting, *Materials*, 12 (2019).
- [31] Y.-j. Li, A.-p. Wu, Q. Li, Y. Zhao, R.-c. Zhu, G.-q. Wang, Effects of welding parameters on weld shape and residual stresses in electron beam welded Ti<sub>2</sub>AlNb alloy joints, *Transactions of Nonferrous Metals Society of China*, 29 (2019) 67-76.
- [32] C. Guoqing, Z. Binggang, L. Wei, F. Jicai, Crack formation and control upon the electron beam welding of TiAl-based alloys, *Intermetallics*, 19 (2011) 1857-1863.
- [33] Al-Nb-Ti (Aluminium - Niobium - Titanium), in: G. Effenberg, S. Ilyenko (Eds.) *Light Metal Systems. Part 3: Selected Systems from Al-Fe-V to Al-Ni-Zr*, Springer Berlin Heidelberg, Berlin, Heidelberg, 2005, pp. 1-46.
- [34] D. Holec, R.K. Reddy, T. Klein, H. Clemens, Preferential site occupancy of alloying elements in TiAl-based phases, *Journal of Applied Physics*, 119 (2016).
- [35] W. Diao, L.-H. Ye, Z.-W. Ji, R. Yang, Q.-M. Hu, Site Occupation of Nb in  $\gamma$ -TiAl: Beyond the Point Defect Gas Approximation, *Acta Metallurgica Sinica (English Letters)*, (2019).
- [36] X.F. Ding, J.P. Lin, L.Q. Zhang, G.L. Chen, Effects of heat treatment on microstructure of directionally solidified Ti-45Al-8Nb-(W, B, Y) alloy, *Transactions of Nonferrous Metals Society of China (English Edition)*, 21 (2011) 26-31.
- [37] L. Song, L.Q. Zhang, X.J. Xu, J. Sun, J.P. Lin, Omega phase in as-cast high-Nb-containing TiAl alloy, *Scripta Materialia*, 68 (2013) 929-932.
- [38] L.A. Bendersky, W.J. Boettinger, B.P. Burton, F.S. Biancaniello, C.B. Shoemaker, The formation of ordered  $\omega$ -related phases in alloys of composition Ti  $\langle$ inf $\rangle$ 4 $\langle$ /inf $\rangle$  Al  $\langle$ inf $\rangle$ 3 $\langle$ /inf $\rangle$  Nb, *Acta Metallurgica Et Materialia*, 38 (1990) 931-943.
- [39] Y. Wen, X. Zeng, Z. Hu, R. Peng, J. Sun, L. Song, A comparative first-principles study of tetragonal TiAl and Ti<sub>4</sub>Nb<sub>3</sub>Al<sub>9</sub> intermetallic compounds, *Intermetallics*, 101 (2018) 72-80.

- [40] L. Hong-Wei, L. Cheng-Ping, Y. Yong, L. Jun-Ming, L. Zhi-Guo, Interpretation of the morphology and crystallography of precipitate  $\gamma_1$ -Ti<sub>4</sub>Nb<sub>3</sub>Al<sub>9</sub> in L1<sub>0</sub>-TiAl(Nb)-based intermetallics by invariant line theory, *Intermetallics*, 15 (2007) 1497-1503.
- [41] C. Kenel, C. Leinenbach, Influence of Nb and Mo on microstructure formation of rapidly solidified ternary Ti-Al-(Nb, Mo) alloys, *Intermetallics*, 69 (2016) 82-89.
- [42] A.V. Kartavykh, Electron microscopy of the primary microstructure of rapidly solidified Ti-46Al-8Nb alloy, *Russian Metallurgy (Metally)*, 2011 (2011) 72-77.
- [43] I.V. Ivanov, A. Thoenmes, V.Y. Skiba, A.A. Ruktuev, I.A. Bataev, Effect of Electron Beam Power Density on the Structure of Titanium Under Non-Vacuum Electron-Beam Treatment, *Metal Science and Heat Treatment*, 60 (2019) 625-632.
- [44] V.Y. Skeebe, V.V. Ivancivsky, N.V. Martyushev, D.V. Lobanov, N.V. Vakhrushev, A.K. Zhigulev, Numerical simulation of temperature field in steel under action of electron beam heating Source, *Key Engineering Materials*, 2016, pp. 105-111.
- [45] F. Perdrix, M.F. Trichet, J.L. Bonnentien, M. Cornet, J. Bigot, Relationships between interstitial content, microstructure and mechanical properties in fully lamellar Ti-48Al alloys, with special reference to carbon, *Intermetallics*, 9 (2001) 807-815.
- [46] A. Klimová, J. Lapin, Microstructure evolution during annealing of cast TiAl-based alloy, *METAL 2014 - 23rd International Conference on Metallurgy and Materials, Conference Proceedings*, 2014, pp. 1145-1150.
- [47] Y. Garip, O. Ozdemir, A study of the cycle oxidation behavior of the Cr/Mn/Mo alloyed Ti-48Al-based intermetallics prepared by ECAS, *J. Alloy. Compd.*, 818 (2020).
- [48] A. Thoenmes, I.V. Ivanov, A.A. Ruktuev, D.V. Lazurenko, I.A. Bataev, Structure and Phase Composition of Biomedical Alloys of the Ti – Nb System in Cast Condition and After Heat Treatment, *Metal Science and Heat Treatment*, 60 (2019) 659-665.
- [49] L. Lutterotti, S. Matthies, H.-R. Wenk, MAUD: a friendly Java program for material analysis using diffraction, *IUCr: Newsletter of the CPD*, 1999, pp. 14-15.
- [50] V.A.C. Haanappel, H. Clemens, M.F. Stroosnijder, The high temperature oxidation behaviour of high and low alloyed TiAl-based intermetallics, *Intermetallics*, 10 (2002) 293-305.
- [51] J.D. Sunderkötter, H.J. Schmutzler, V.A.C. Haanappel, R. Hofman, W. Glatz, H. Clemens, M.F. Stroosnijder, The high-temperature oxidation behaviour of Ti-47Al-2Cr-0.2Si and Ti-48Al-2Cr-2Nb compared with Ti-48Al-2Cr, *Intermetallics*, 5 (1997) 525-534.
- [52] Y. Shida, H. Anada, The effect of various ternary additives on the oxidation behavior of TiAl in high-temperature air, *Oxidation of Metals*, 45 (1996) 197-219.
- [53] M.F. Stroosnijder, N. Zheng, W.J. Quadackers, R. Hofman, A. Gil, F. Lanza, The effect of niobium ion implantation on the oxidation behavior of a  $\gamma$ -TiAl-based intermetallic, *Oxidation of Metals*, 46 (1996) 19-35.
- [54] Y. Shen, X. Ding, F. Wang, Y. Tan, J.M. Yang, High temperature oxidation behavior of Ti-Al-Nb ternary alloys, *Journal of Materials Science*, 39 (2004) 6583-6589.
- [55] M. Yoshihara, K. Miura, Effects of Nb addition on oxidation behavior of TiAl, *Intermetallics*, 3 (1995) 357-363.
- [56] *Titanium and titanium alloys. Fundamentals and application.*, Wiley-VCH, 2003.
- [57] A. Ralison F Dettenwanger, M. Schütze, Oxidation of orthorhombic Ti<sub>2</sub>AlNb alloys at 800 °C in air, *Werkstoffe und Korrosion*, 51 (2000) 317-328.
- [58] G.H. Meier, Research on oxidation and embrittlement of intermetallic compounds in the U.S, *Materials and Corrosion - Werkstoffe und Korrosion*, 47 (1996) 595-618.
- [59] S. Karthikeyan, G.B. Viswanathan, M.J. Mills, Evaluation of the jogged-screw model of creep in equiaxed  $\gamma$ -TiAl: Identification of the key substructural parameters, *Acta Materialia*, 52 (2004) 2577-2589.
- [60] S. Karthikeyan, G.B. Viswanathan, P.I. Gouma, V.K. Vasudevan, Y.W. Kim, M.J. Mills, Mechanisms and effect of microstructure on creep of TiAl-based alloys, *Materials Science and Engineering: A*, 329-331 (2002) 621-630.

- [61] G.B. Viswanathan, S. Kartikeyan, M.J. Mills, V.K. Vasudevan, Creep properties of a fully-lamellar Ti-48Al-2Cr-2Nb alloy, *Mat. Sci. Eng. A*, 319-321 (2001) 833-837.
- [62] P. Hitier, J.L. Bonnentien, C. Bertrand, M. Cornet, J. Bigot, Influence of purity level on the structural evolution and the mechanical properties of the Ti-48Al alloys, *Physica Status Solidi (A) Applied Research*, 160 (1997) 541-547.
- [63] M. Sujata, D.H. Sastry, C. Ramachandra, Microstructural characterization and creep behaviour of as-cast titanium aluminide Ti-48Al-2V, *Intermetallics*, 12 (2004) 691-697.
- [64] H.Y. Kim, S.H. Hong, The effect of microstructures on creep behavior of Ti-48Al-2W intermetallic compounds, *Mat. Sci. Eng. A*, 329-331 (2002) 788-794.